©2023. This manuscript version is made available under the CC-BY-NC-ND 4.0 license https://creativecommons.org/licenses/by-nc-nd/4.0/. This is the accepted version of "Design, development and testing of 3D-printed conformal energy absorbing structures" published Materials Today Communications, Volume 35, 18 May 2023, 106204. Available online via https://doi.org/10.1016/j.mtcomm.2023.106204.

Design, development and testing of 3D-printed conformal energy absorbing structures

Corresponding Author

Silvio Schröder, DLR German Aerospace Center, Institute of Space Systems, Robert-Hooke Str.7, 28359 Bremen, Germany, Silvio.schroeder@dlr.de

Co-Authors

Christian D. Grimm, DLR German Aerospace Center, Institute of Space Systems Robert-Hooke Str.7, 28359 Bremen, Germany, Christian.Grimm@dlr.de

Lars Witte, DLR German Aerospace Center, Institute of Space Systems, Robert-Hooke Str.7, 28359 Bremen, Germany, Lars.Witte@dlr.de

Adli Dimassi, Faserinstitut Bremen e.V., Bremen, Am Biologischen Garten 2, 28359 Bremen, Dimassi@faserinstitut.de

Philip Buchholz, Materialise GmbH, Fahrenheitstr. 1, 28359 Bremen, Germany, Philip.Buchholz@materialise.de

Abstract

Landing a spacecraft on a foreign body is a key challenge to explore new worlds. Besides the task of approach and decent the landing has to nullify the residual kinetic energy. For large or medium-sized landers this will be done by the landing gear with shock absorbers inside the landing legs. For small landers alternative ways of reducing the shocks of the touchdown have to be developed, since the landing gear has a higher mass fraction when the lander gets smaller.

A suitable method for protecting a lander from the shock of impact is a crushable shell, which absorbs the kinetic energy at touchdown by plastic deformation of its core material.

The core material is commonly made of aluminum honeycomb which is very lightweight and has a constant energy dissipation characteristic. On the other hand, the materials stiffness strongly relates to the direction of load, since tilted load transfers reduce the energy absorptivity drastically. This applies specially for landers with no active guidance and control ability. In those cases, the entire vehicle has to be covered with crushable elements with the honeycomb cells aligned accordingly.

A new and innovative method of omni-directional crash protection is a metal grid which can be manufactured additively. With this feature the lander can land in any inclination without losing crush performance.

In this paper the development of a 3D-printed energy absorbing structure is presented. Hardware tests have shown the effectiveness of this method in comparison to the benchmark of honeycomb shock absorbers.

Keywords

Additive manufacturing, crushable structures, honeycomb shock absorbers, impact testing, Landing & Mobility Test Facility

1. Introduction / Motivation

When moving structures approach an obstacle and collide with it intentionally or unintentionally, it is necessary to reduce the remaining speed as gently as possible in order to protect the cargo (payload) from excessive acceleration. Therefore, vehicles are built in such a way that, in the event of an impact, certain designated areas of the vehicle deform plastically, thus removing kinetic energy from the system. Examples are collapse zones in trains [1] or bumper beams in cars [2]. Moreover, crushable materials like aluminum honeycombs [3] or metal foams [4],[5] can be used to design lighter and more efficient absorbers for impact protection.

Honeycombs are known to have a very high specific energy, as they are very light and can dissipate a lot of energy through their controlled crumbling of cells. However, they can do this primarily in one cell direction only. If forces are applied crosswise, the materials resistance is much weaker and it can no longer absorb any significant energy. Metal foams have the advantage of compressing equally in any load direction, but they are inferior in terms of overall weight, available low stiffnesses and reproducibility.

Good alternatives are presented by 3D-printed metal structures, which can be built multi-directionally, have good reproducibility, and acceptable energy absorption capabilities [6].

As an example, this paper describes the protection of a spacecraft that is to land on a small solar system body (e.g. asteroids, comets). Referring to the boundary conditions of a small lander (≈15kg), solutions such as thrusters (for a soft touchdown) or landing legs are discounted because they would increase the structural mass significantly. Parachute landings are also not possible on small bodies due to the lack of an atmosphere. However, to protect the lander from a severe impact, its primary structure needs to be covered by an energy-absorbing damping structure. This protective structure has to surround the entire lander, since it has no attitude control to stabilize the lander during the landing approach and can impact in any conceivable orientation.

The later chapters will go into detail concerning the development of a lander test model with 3D-printed impact elements (chapter 2), including material selection and the design of the core lattice structure. The challenges of manufacturing the crash elements are discussed in chapter 3. In chapter 4 the experimental investigation of the produced specimens is presented and results of expressive test cases are shown. Each case is compared to the performance of conventional honeycomb impact absorbers.

1.1. Baseline of a crushable protection system

For the implementation of a demonstrator, a generic 15 kg lander was designed, capable of effectively decaying the residual velocity without putting too much stress on the primary housing and its internal instruments. For this, two possible lander versions were derived: the first with a fully 6-sided enclosure, and the second using a flywheel for horizontal stabilization, featuring a platform with only one crushable element (Fig. 1-1). Depending on the alternative used, the protective structure can be either unfolded or ejected after landing to give the lander a clear field of view for science and communication. In each case, the crushable shell pieces, a.k.a. crash-pads, consist of a crushable core glued to a stiff baseplate and wrapped in a composite face-sheet.

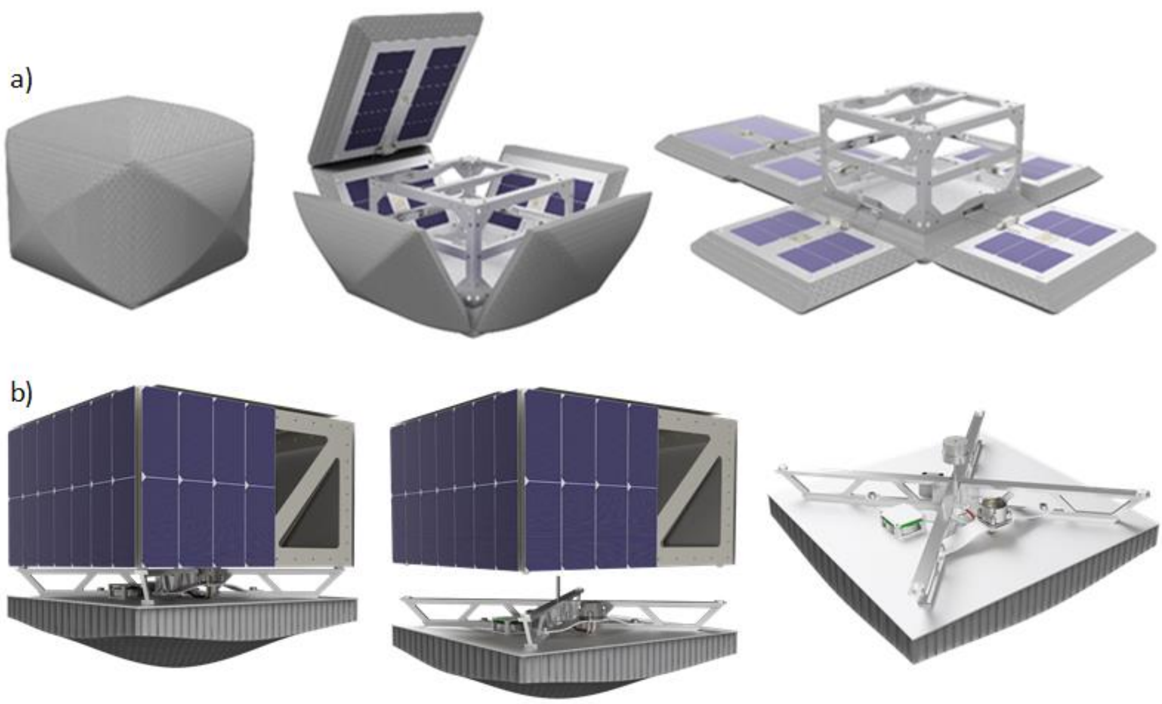

Fig. 1-1: Depiction of 2 possible lander configurations: a) a fully-6-sided protection enclosure, and b) a horizontally stabilized version with single side protection. Images from left to right: free fall and touchdown configuration to post landing configuration.

In general, the most important parameter for the design of an impact absorber is its thickness. A crash-pad should be sufficiently thick to provide enough material that can be compressed without reaching its densification limit, but it should also not carry too much extra material so as to be as lightweight as possible. The indentation profile here is mainly dependent on the impacting obstacle. With the addition of a limiting face-sheet, the deformation then follows the theory of plates and shells [7]. The indentation profile here roughly resembles a Gaussian function or a symmetrical bell-shaped curve, which cannot easily be determined [8]. A more practical, though conservative, approach would be to neglect the positive effect of the face-sheet initially and to perform an estimation based on simple obstacle geometry. During an impact, the kinetic impact energy of an object with mass *m* and velocity *v* is dissipated by the deformed volume *V_cr* of the crushable material with its crush strength *σ_cr*:

$$½\, m \cdot v^2 = \sigma_{cr} \cdot \overbrace{A \cdot s_{cr}}^{V_{cr}} \quad \text{(Eq. 1.1)}$$

An impactors height (with cross section or crush area *A*) then equals the penetration/ deceleration distance *s_cr*. This simple fact can be used to determine the required minimal thickness t_{min} of a crushable impact absorber. Fig. 1-2 lists three possible boulder geometries (crush volumes) including a half-sphere, half-spheroid and a combined volume of a half-sphere plus cylinder segment.

	Boulder type	Crush volume	Constraints	h = s = t_{min}
B1	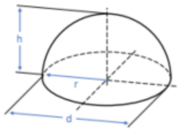	$V_{cr} = \frac{2}{3}\,\pi\, r^3$	$r = h$	$h = \sqrt[3]{\frac{3\, mv^2}{4\, \sigma_{cr}\pi}}$
B2	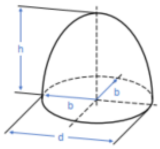	$V_{cr} = \frac{2}{3}\,\pi\, b^2\, h$	$b = c\, h$	$h = \sqrt[3]{\frac{3\, mv^2}{4\, \sigma_{cr}\pi c^2}}$
B3	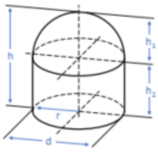	$V_{cr_1} = \frac{2}{3}\,\pi\, h_1^3$ $V_{cr_2} = \pi\, r^2\, h_2$	$h_2 = c\, h_1$ $h = h_1 + h_2$	$h_1 = \sqrt[3]{\frac{mv^2}{2\, \sigma_{cr}\pi\left(\frac{2}{3}+c\right)}}$ $h = h_1\,(1 + c)$

Fig. 1-2: Derivation of the minimal thickness tmin for an impact absorber based on resulting obstacle geometries.

For an independent and closed solution, some constraints need to be defined. The height of the half-sphere boulder (B1) is equal to its radius, whereas the width of the half-spheroid boulder (B2) is set as a function of its height defined by the form factor c. If this factor is smaller than 1, the resulting crush volume will produce a prolate (or pointy) imprint. If the factor is greater than 1, the resulting crush volume will produce an oblate (or blunt) imprint. In a similar way, the height of the cylinder segment for the half-sphere plus cylinder boulder (B3) is set in relation to the height/radius of its top half-sphere defined also by the form factor c. The greater the form factor here, the longer and thinner the resulting imprint will become. The mathematical boundaries can be found by setting c equal to 0 for B3 and to 1 for B2, which will lead in both cases to a half-sphere volume and therefore to the same crush imprint and distance as B1. Inserting these volumes into Equation 1.1 and solving for the respective height will finally provide the minimal thickness.

The only required material constant here is the crush strength σ_{cr}. This is found by a defined limiting acceleration load G for a particular landing system (mission or system requirement), using the force law F = m*a, where a=g*G and σ=F/A, which leads to

$$\sigma_{cr} = \frac{m \cdot g \cdot G}{A} \quad \text{(Eq. 1.2)}$$

and solving for the maximal expected crush area of a flat impact case. If the required crush strength is not available from a selected manufacturer, the closest lower crush strength to the one needed should be used. If it is too small and no such soft material is available at all, the contacting face will need to be limited by a geometrical adaptation of the absorber design (e.g. curved contour). This approach will provide a quick, reasonable and "safe" absorber thickness, which can be built and tested or used as initial dimensioning for further optimization in a more detailed FE analysis.

2. Design and Development

Several materials were identified for the metal grid structure and cover layers; their properties were evaluated and a suitable material was selected for each application.

2.1. Materials for 3D-printed lattice structure

Three materials were available for the production of the lattice structure: aluminum (ALSi10Mg) on a SLM 500 machine, stainless steel (316L) and titanium (TiAl6V4) on EOS M280. The material properties such as density, Young's modulus and yield strength and the processing of the material were the criteria for the selection process. When considering the mechanical criteria, titanium is the most suitable material for the crushable structure. Steel has the highest yield strength, which is an important factor for plastic deformability, while aluminum is the easiest to handle, and the most common 3D-printing machines are also designed for aluminum. In the end, all three materials were tested for their suitability.

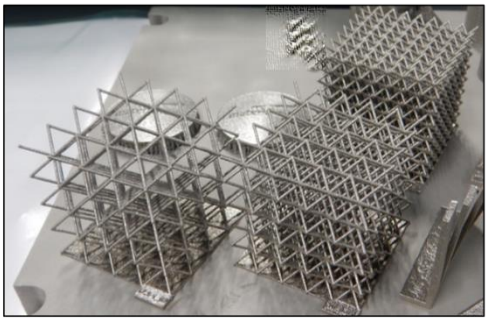

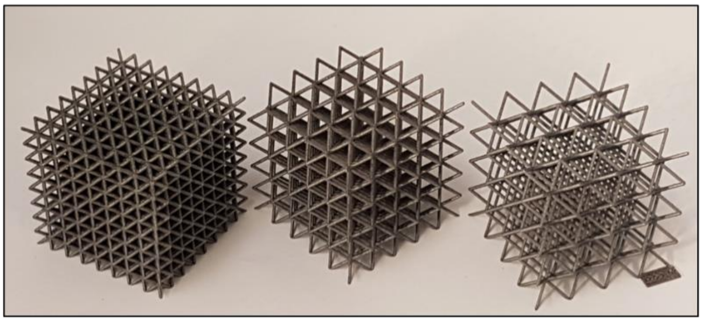

Fig. 2-1: 3D-printed stainless-steel specimens

After test specimens for all three materials were printed (Fig. 2-1), they were examined in a compression testing machine for their plastic behavior (see Fig. 2-5). It was found that both aluminum and titanium are unsuitable for absorbing kinetic impacts. The rods of the test specimen buckled first under compression, but instead of deforming plastically as intended, they broke due to their brittle characteristics. Hence, energy could not be dissipated in deformation work. Stainless steel, however, showed the desired plastic deformation under compressive loads. For this reason, it was the only material suitable for additive manufacturing of metal grids to be used as energy absorbers in the frame of the given project.

Other studies revealed the possibility of increasing the compression ductility of aluminum alloys up to 90% with certain heat treatments [9]. However, a reduction in strength of the treated material of 40-50% has to be considered.

Only classic materials such as metals were considered in this investigation. Exotic alternatives such as liquid crystal elastomers [10] were not included in the selection because the database is not meaningful enough and the focus in this work was on 3D-printed metal meshes.

2.2. Materials for the top layer

In order to select a cover material with good impact properties, semi-finished fiber products with high elongation at break, such as ultra-high-molecular-weight-polyethylene (Dyneema®), aramid fiber (Kevlar®) and glass fiber, were compared with each other. Due to the poor impact properties of carbon fibers, they were not included in the comparison. The decisive factors for selecting a suitable material were the thermal and UV resistance as well as the processability of the fiber semi-finished product. Comparison of the materials showed that the glass fiber fabrics represent a good compromise between mechanical properties, cost and processability. For the further course of the project, the glass fabric Aero, Finish FK 144, and canvas with a basic weight of 163g/m² from the company Interglas was used in combination with the laminating resin Epikote Resin MGS LR160/Epikure Curing Agent MGS LH160 from the company Hexion.

2.3. Design of an energy absorbing metal grid

The core component of the energy-absorbing lattice is the elementary cell. Suitable cells could be selected from an existing portfolio for initial tests. For mechanical tests, a cube with an edge length of 50mm was provided with a grid structure. Here, the density and rod diameter as well as the material and geometry of the unit cell are variables, which would influence the energy absorption behavior of the crushing structure. To provide an initial assessment of the crush behavior, three different lattice structures were created and printed in the different materials. The edge length of the cube was kept the same at 50 mm to provide a comparable evaluation.

The population can be made with different densities. To obtain four whole elementary cells in one axis of the cube, the dimensions 12.5 x 12.5 x 12.5 mm per unit cell are required. Doubling the number leads to dimensions of 6.25 x 6.25 x 6.25 mm per unit cell. Since a too dense grid is already created here, an intermediate solution with the size 10 x 10 x 10 mm was selected as the third version. The example with the elementary cell "Dense" is used to generate the geometry (Fig. 2-2).

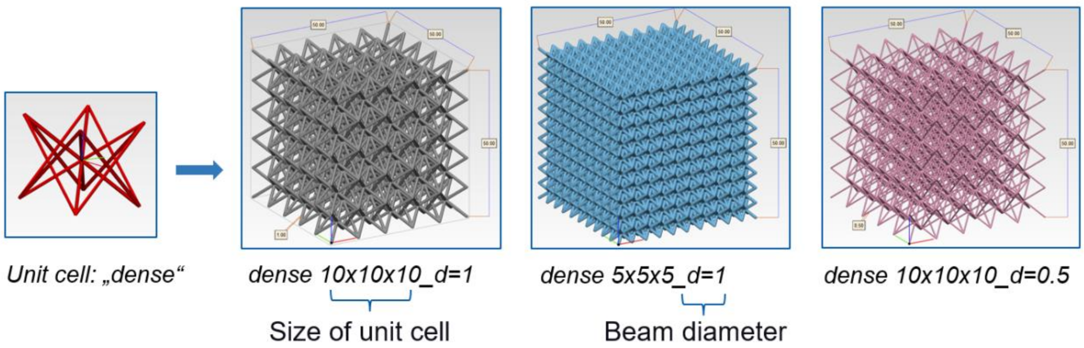

Fig. 2-2:Three examples of lattice structures with unit cell "Dense"

The first results from the tests provided information about the behavior of a lattice structure in different materials. For these tests, the unit cell Cell_00 ("Diagonal") was chosen and populated in the cube according to the principle described above.

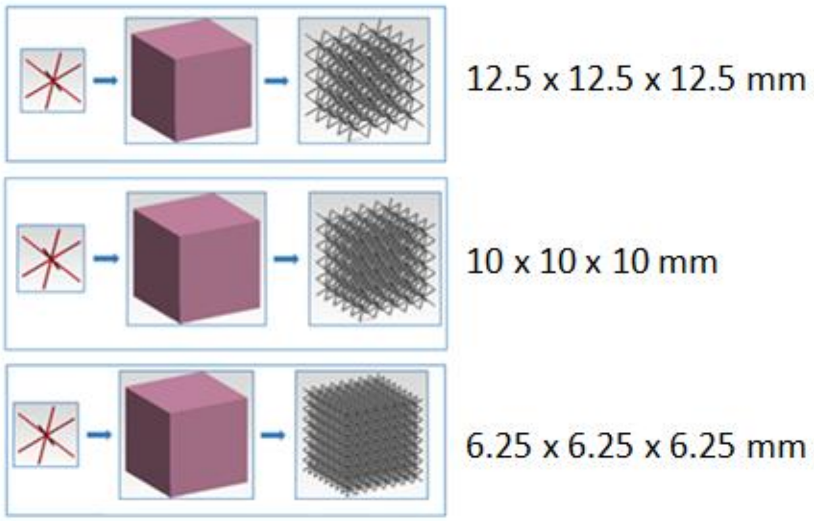

Fig. 2-3: "Diagonal" unit cell with different densities.

The "Diagonal" unit cell is simpler than the "Dense" cell. This makes it easier to understand the crushing behavior during deformation. In addition, this cell is best suited for 3D printing, since the proportion of overhangs is reduced compared to other cells.

In order to consider, as far as possible, only one component of the four variable influencing factors as actually variable, the factor "elementary cell" was thus already definite for the time being. In addition, the printing process requires a minimum rod diameter of 1 mm. That is why this value was chosen. The two remaining variables "Density" and "Material" were tested as described, so that only one factor was changed in each case.

In addition, the density of the unit cell arrangement was varied to produce three different test specimens. In order to obtain four whole unit cells in one axis of the cube, the dimensions were set to 12.5 x 12.5 x 12.5 mm, 6.25 x 6.25 x 6.25 mm and 10 x 10 x 10 mm per unit cell (see Fig. 2-3). Each cube has dimensions of 50 x 50 x 50 mm.

2.3.1. Mechanical characterization of metal lattice structures and surface layers

For a more detailed investigation, uniaxial compression tests were performed according to the DIN 53291 standard. Four metal grid specimens (Fig. 2-4) with four different cell densities were tested. From the measured force-displacement diagrams (Fig. 2-5), the material characteristics, such as compressive strength and absorbed energy, were determined. An advantage of 3D printed metal grids is the high flexibility of the internal cell structure and its buildup. With this, varying densities with interconnected transitions as well as quasi-isotropic compression characteristics can be achieved. However, as the tests performed in this paper show, there can also be a load axes dependency for printed structures when simple seed unit cells are used with e.g. straight rods and orthogonal nodes (see Fig. 2-3). Here, the anticipated compressive strength is valid only in the nominal compressive axis, where the metal rods are at an angle of 45 degrees, enabling them to bend according to classic beam theory. If, however, the compression is applied under a 45-degree angle, the force vector is aligned with the rods. As a consequence, they do not bend but rather behave as a solid material (buckling problem). Hence, such a metal structure would be isotropic only in its principal axes (X, Y, Z), but would feature a significant (possibly exponential) increase in its stiffness for all other loading angles. This characteristic will be investigated in more detail in future studies.

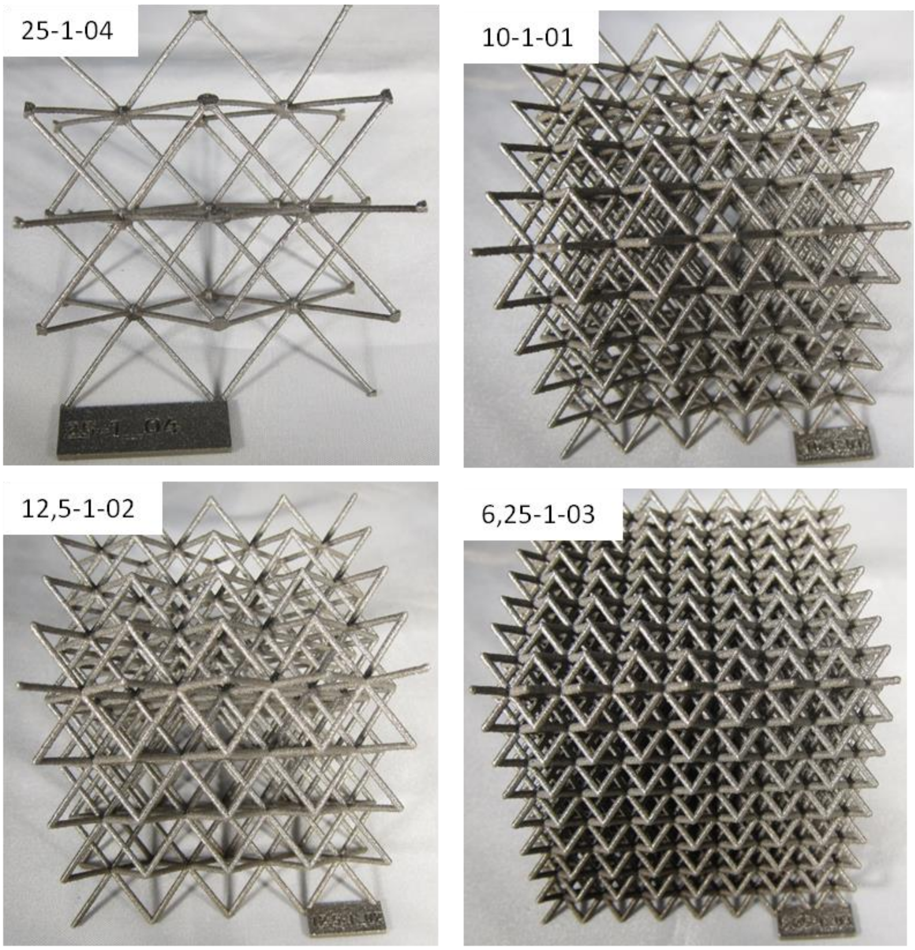

Fig. 2-4: Tested stainless steel metal grid structures.

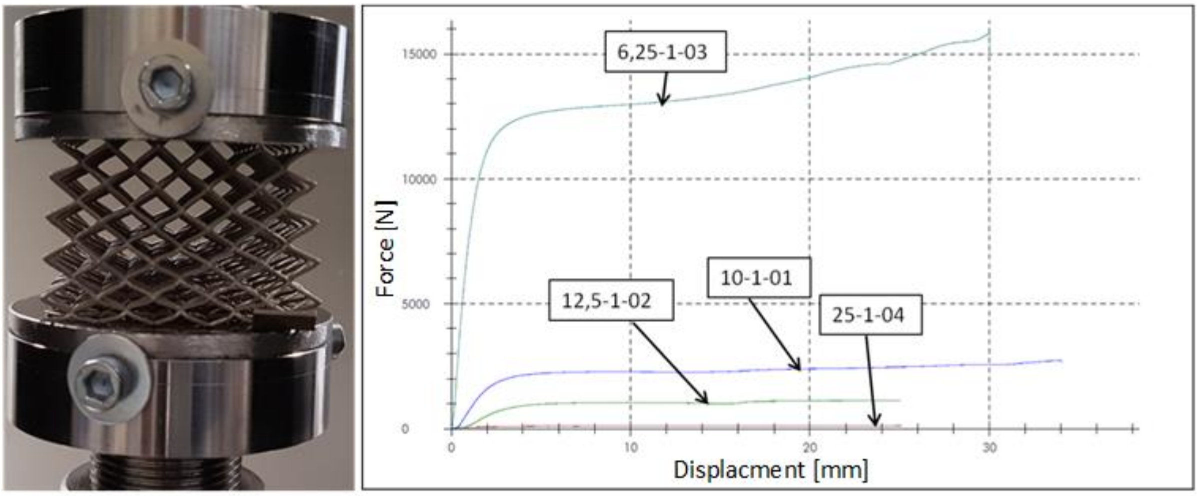

Fig. 2-5: Force-displacement curves of the tested metal lattice structures.

For the nominal case of an applied load in one of the principal axes, the determined material characteristics are shown in Table 2-1. The results show that the crush strength and energy absorption capability increase exponentially with the increase in cell density. These test results are also depicted in Fig. 2-7 (magenta colored, diamond symbol). The parameter of the exponential relation between the sample's bulk density and crush strength is obtained by regression, whose curve is shown as well. For comparison, similar data from commercially available aluminum honeycomb grades (data and references are given in the annex of this paper) are plotted together with their associated regression curves. This data includes the material grades with the lowest available crush strength. The printed (steel alloy) lattice samples show at first a significant, by one order of magnitude, disadvantage of its bulk density. The lowest crush strength value of 0.035 MPa (25 mm unit cell) matches the lowest honeycomb crush strength. The honeycomb crush force refers to its stronger major axis T, which is in line with the cell openings (Fig. 2-6).

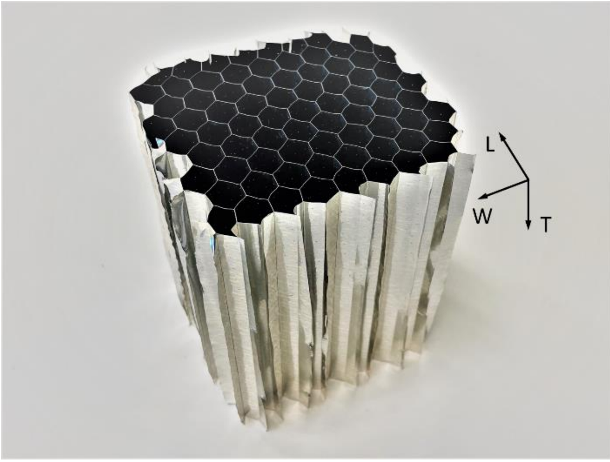

Fig. 2-6: Cell structure of expanded aluminum honeycomb.

The printer machine used supports the production of even larger, less dense lattice unit cells. Therefore, the theoretical bulk density of a 50 mm size unit cell was extrapolated from the tested samples (dotted magenta line and square symbol in Fig. 2-7). This suggests that the realization of crush strength figures of one order lower than the lowest honeycomb grades would have been possible. For the further investigations in the frame of this study, a mass optimized 23 mm unit cell, still using the same steel alloy but featuring a reduced connecting node between the pins, was manufactured. A test sample was produced for the chosen 23 mm lattice as well, and the characteristics can also be found in Table 2-1 (specimen 23-1-10) and Fig. 2-7 (red circle symbol). The compressive strength fits with the previously produced samples, but has significant advantages in its density. All the manufacturing- and testing- processes in the following course of this paper is based on this unit cell size.

Table 2-1: Material characteristics of the stainless steel and honeycomb grid structures.

Specimen	**Young's modulus [MPa]**	**Compressive strength [MPa]**	**Energy [J]**	**Spec. Energy [J.m³/kg]**	**Density [kg/m³]**
25-1-04	0.563	0.035	2.3	0.02	115.5
12,5-1-02	7.692	0.38	24.0	0.09	257.9
10-1-01	21.08	0.85	53.3	0.14	391.6
6,25-1-03	180.8	4.87	314.8	0.33	942.6
23-1-10	0.533	0.037	6.2	0.11	56.4

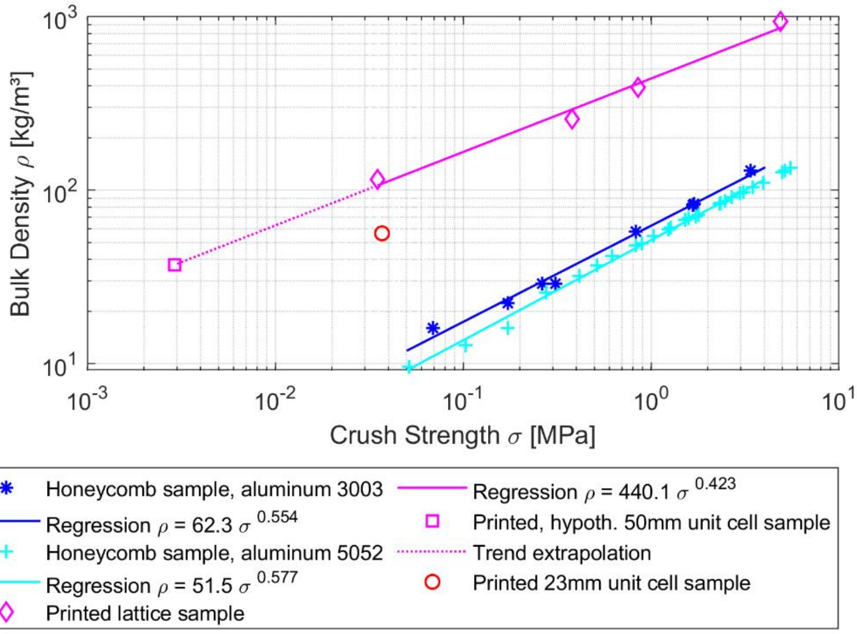

Fig. 2-7: Regression curves of exponential relation between sample's bulk density and crush strength.

The top layer of Aero glass fabric, Finish FK 144, was characterized by means of tensile tests (DIN EN ISO 527-4 and DIN EN ISO 14129) and 3-point bending (3PB) tests (DIN EN ISO 14125) (Fig. 2-8). The determined material characteristics are used in the simulation of the crushable structure. The determined cover layer characteristic values are shown in Table 2-2.

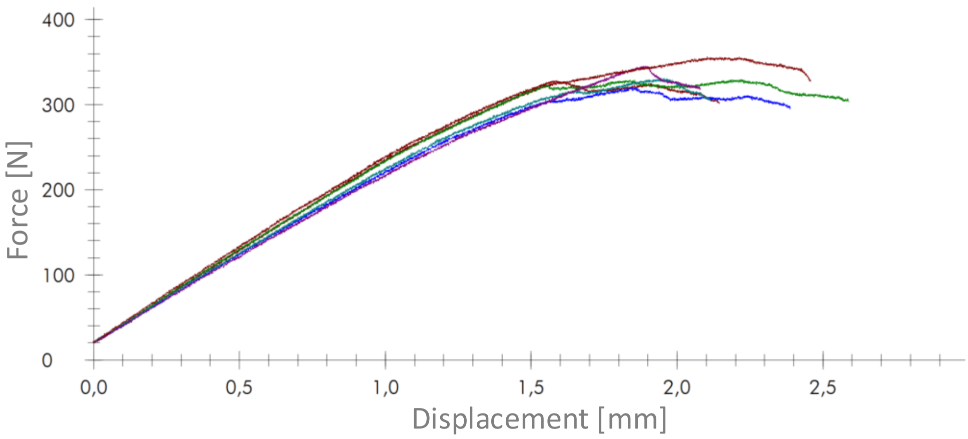

Fig. 2-8: Force displacement curves for 3PB-test (each curve represents one specimen of Aero glass fabric with the same properties).

Table 2-2: Material properties of the surface layer

Youngs modulus [MPa]	**Tensile strength [MPa]**	**ϑ_{12} [-]**	**Shear modulus [MPa]**	**Shear strength [MPa]**
21485	313	0,11	2746	61

3. Manufacturing of absorber crash-pads

Once the geometry of the cushions was defined and a unit cell of the grid structure was established, the file could be prepared for printing. Due to manufacturing restrictions, the outer dimensions here required the cushion to be divided. The small cushions were halved and the large cushions were quartered. Fig. 3-1 shows a quarter on the build platform.

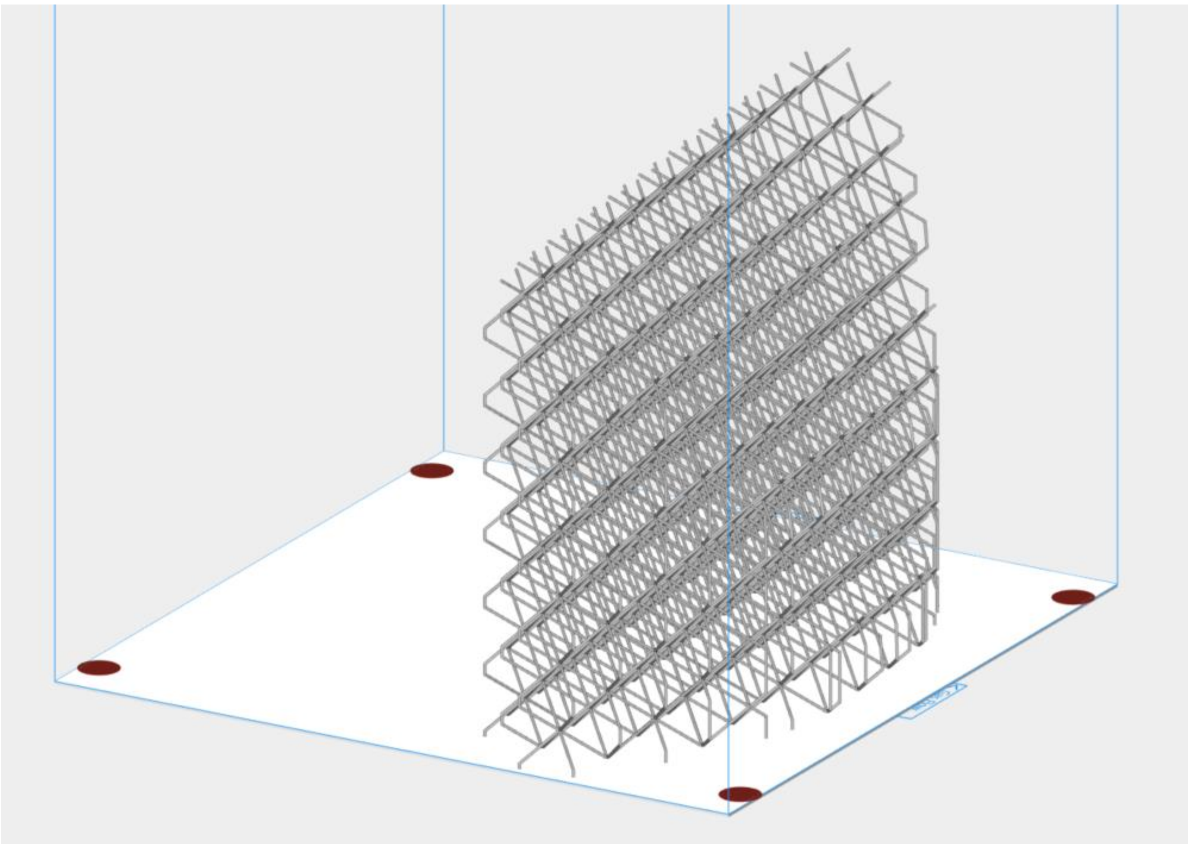

Fig. 3-1: Grid structure (quarter) on building platform.

To avoid support structures, the component orientation is of great importance. The unit cell is self-supporting, so that the orientation of the cushion quarter is predetermined. However, the curved surface of the cushions creates so-called "air-pins". Fig. 3-2 (left) shows a sketch of what air-pins look like. Since the layered printing process causes downward pointing grid bars to start as an "island" in the loose powder bed, they would be pushed away by the recoater. Therefore, it is necessary to remove the air-pins or extend the structure so that it is self-supporting.

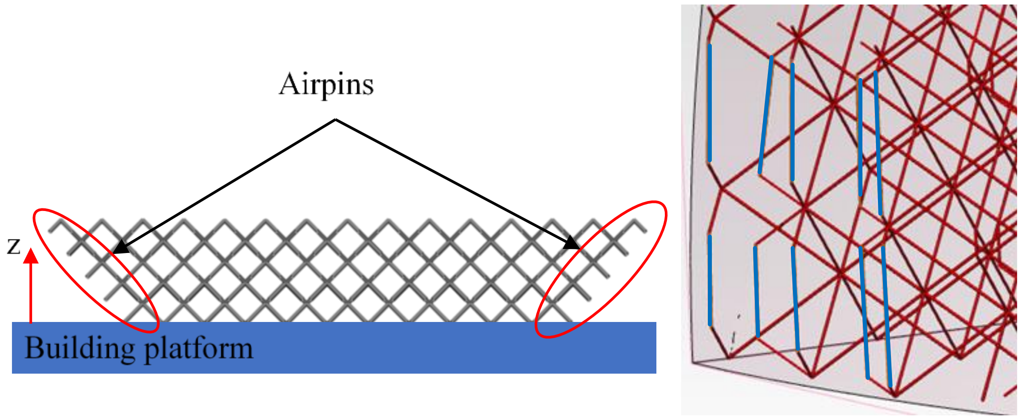

Fig. 3-2: Left: sketched representation of air-pins, right: additional grating bars to avoid air-pins.

The air-pins of the cushions to be printed were supported by 3-matic, Materialise's proprietary software, by inserting additional lattice bars. The software automatically calculates the necessary support structures and adds them [9, chapter 1.34]. In Fig. 3-2 (right), the additional bars are marked in blue. They are self-supporting and can be created by an automatic function in 3-matic.

After printing with the parameters developed by Materialise such as: laser speed, focus size, energy intensity as well as exposure strategy, layer thickness and about 100 other influencing factors, the component is not sandblasted, contrary to the standard process. The sandblasting process would smooth the surface, but this process cannot be defined numerically and does not allow reproducibility.

The production of the metal grids (or core) is organized using the "*Streamics*" software developed by Materialise. The construction jobs are illustrated for capacity and a utilization overview and the component production is planned. The pure printing time of the cushions is about 15 hours. However, press preparation and rework also take up a considerable amount of production time. For example, for preparation, the "hatching strategy", i.e. the path of the laser for sintering surfaces, is selected so that as little internal stress as possible is created, but the mechanical properties reach their optimum. For the separation of the component from the base plate by the wire eroder, another 2 hours are required. To ensure reproducibility, the components are manufactured using the same technology as in the predefined unit cell.

As a special additional process, the core elements had to be welded, since the existing printers are too small for an entire cushion (Fig. 3-3). It must be mentioned that welding has an impact on the material behavior, but this could not be studied in the scope of this project.

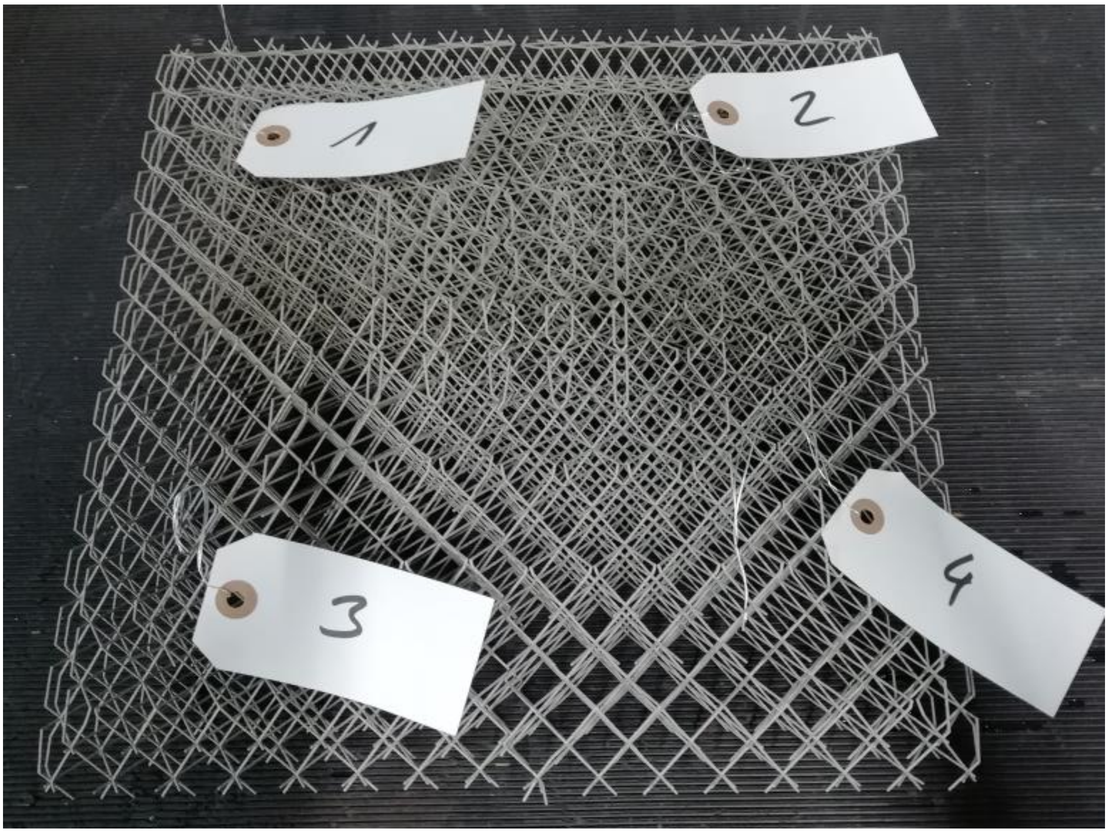

Fig. 3-3: Printed quarter of a large cushion.

The welding of the core halves or quarters was carried out by a subcontractor, who welds the individual bar elements that meet each other by means of the laser welding process. Fig. 3-4 illustrates the manufacturing steps.

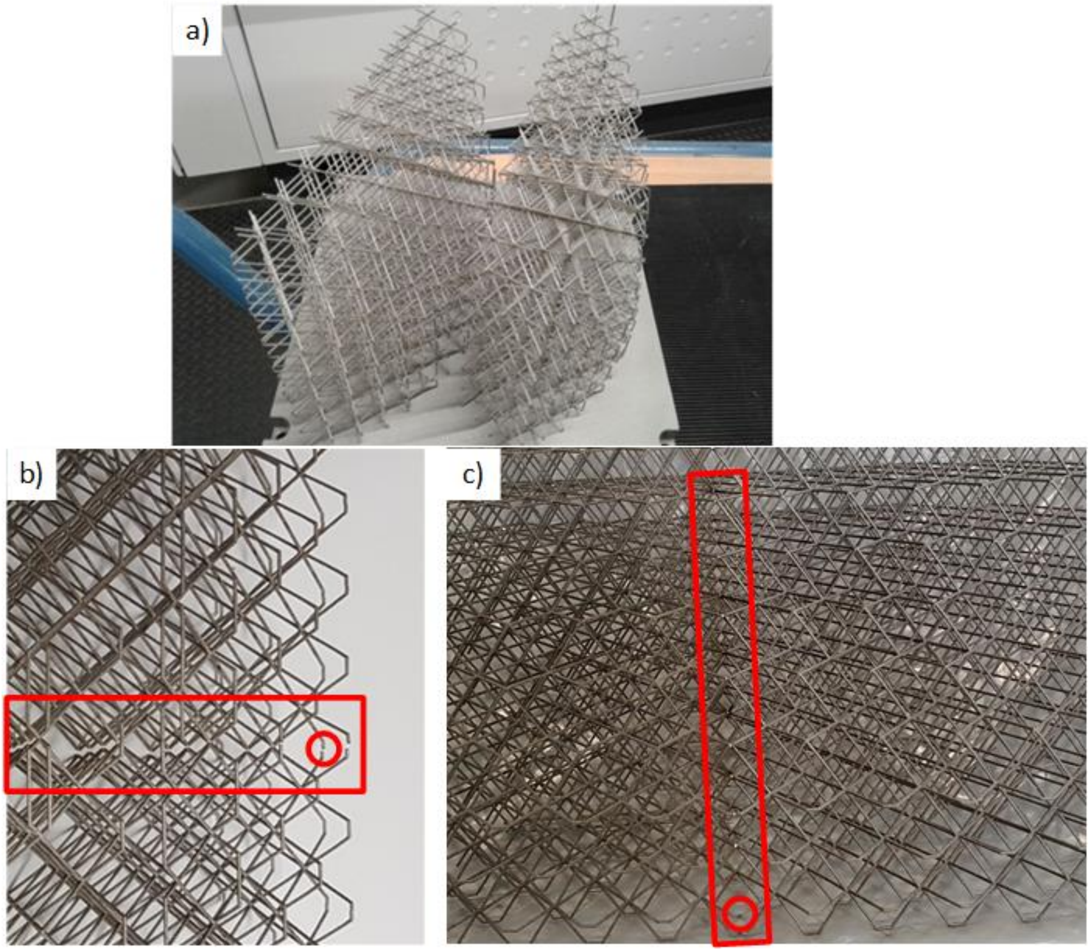

Fig. 3-4: a) Two core halves, b) Lattice bars meeting each other, c) Welded nodes (red rectangle depicts the area of welding, red circle an example of one welding spot).

For the production of the crash cushions (core+cover layers), the geometry of the cushions and the shape of the core are decisive for the selection of the manufacturing process. The geometry is divided into two parts: an upper side with the curved contour and a lower side with the sloping sides and bottom. The CAD drawing of the crash-pads was used to derive the drawings of the laminating molds. Due to the open structure of the lattice core, the cover layers (top and bottom sides) must be produced separately using the vacuum-assisted hand lay-up process. Then, the cores are bonded to the top layers using a mixture of epoxy resin and cotton flocks under vacuum. Finally, the edges are sanded and closed with a GRP strip.

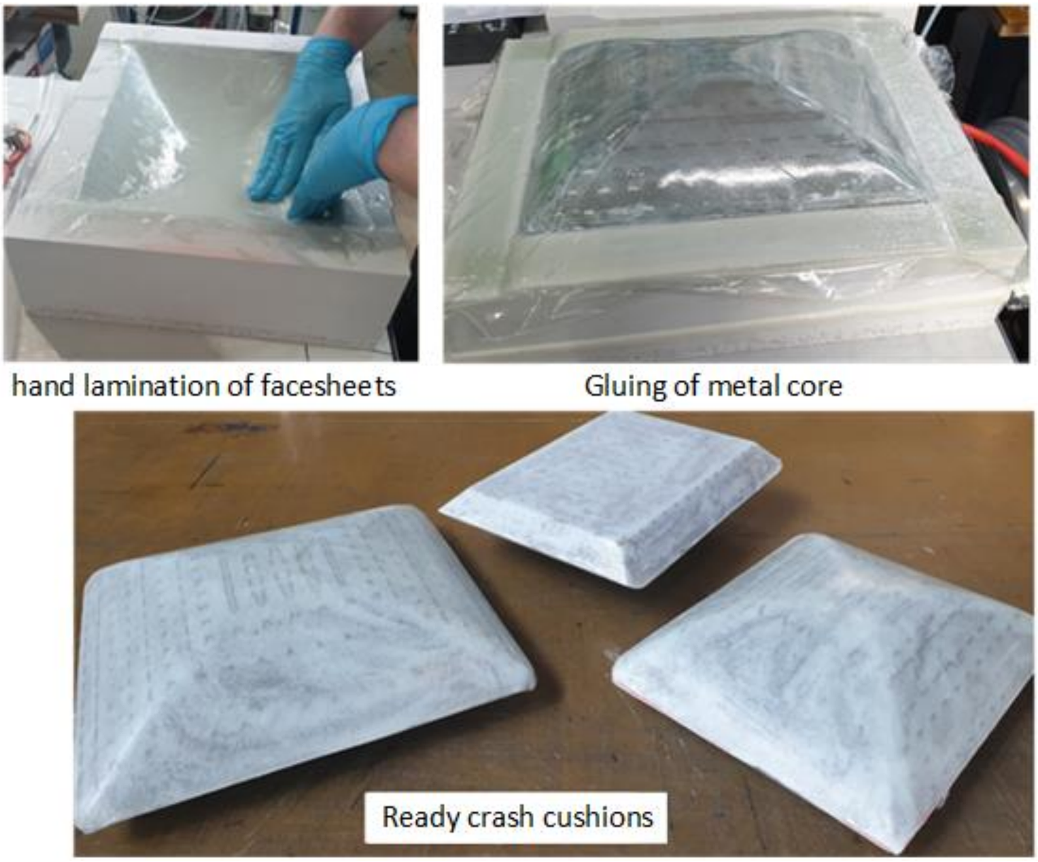

Fig. 3-5: Manufacturing of crash cushions.

The aluminum honeycombs, as reference structure, were machined to obtain the curved shape. Fig. 3-6 shows the associated challenges of machining such thin-walled foil structures, which led to "fraying" of the cut surfaces.

Fig. 3-6: Comparison of aluminum honeycomb cushion after contour milling (left) and after face-sheet lamination (right).

Fig. 3-7 shows a complete setup with six crash cushions made of metal grid cores. It shows the condition after landing and after deployment. In comparison, a separation of the shell with honeycomb core is shown in Fig. 3-8.

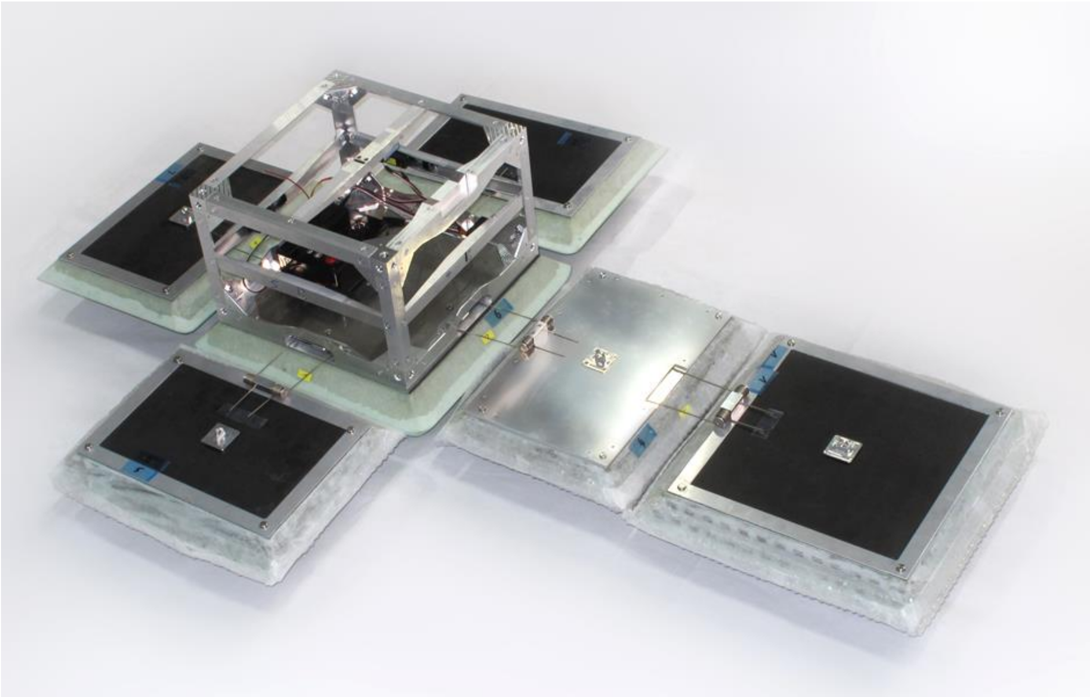

Fig. 3-7: Assembled overall assembly in unfolded state.

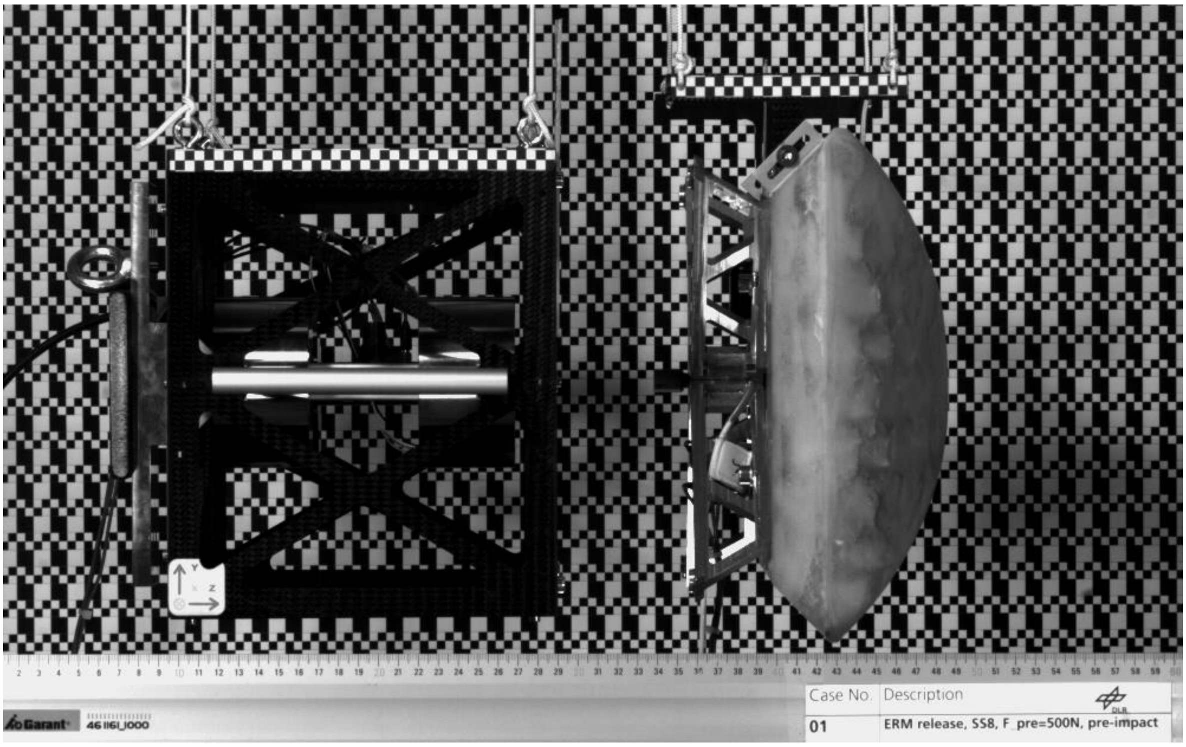

Fig. 3-8: Shell Lander Separation Test.

4. Experimental investigation of the impact characteristics

In order to investigate the mode of action and impact characteristics, tests were carried out with the prototypes described above. The printed structures are compared with classically manufactured honeycomb cushions of otherwise identical design (Fig. 3-6). For this purpose, the test object suspended from a pendulum was accelerated selectively in different orientations against a rigid wall or a rigid impactor. The intention was to simulate the impact on the surface of a celestial body by neglecting gravitational forces. The honeycomb tests are described in [12] and are used here for comparison purposes. The test stand at DLR's Landing & Mobility Test Facility (LAMA) in Bremen (see Fig. 4-1) is also described in detail in [12].

After successful integration into the test rig, the test body was trimmed so that the total effective mass including parts of the pendulum was exactly 15 kg. The sensor technology was focused on force, acceleration and displacement transducers in order to make qualitative statements about the performance of the crash cushions. High-speed video cameras additionally documented the tests.

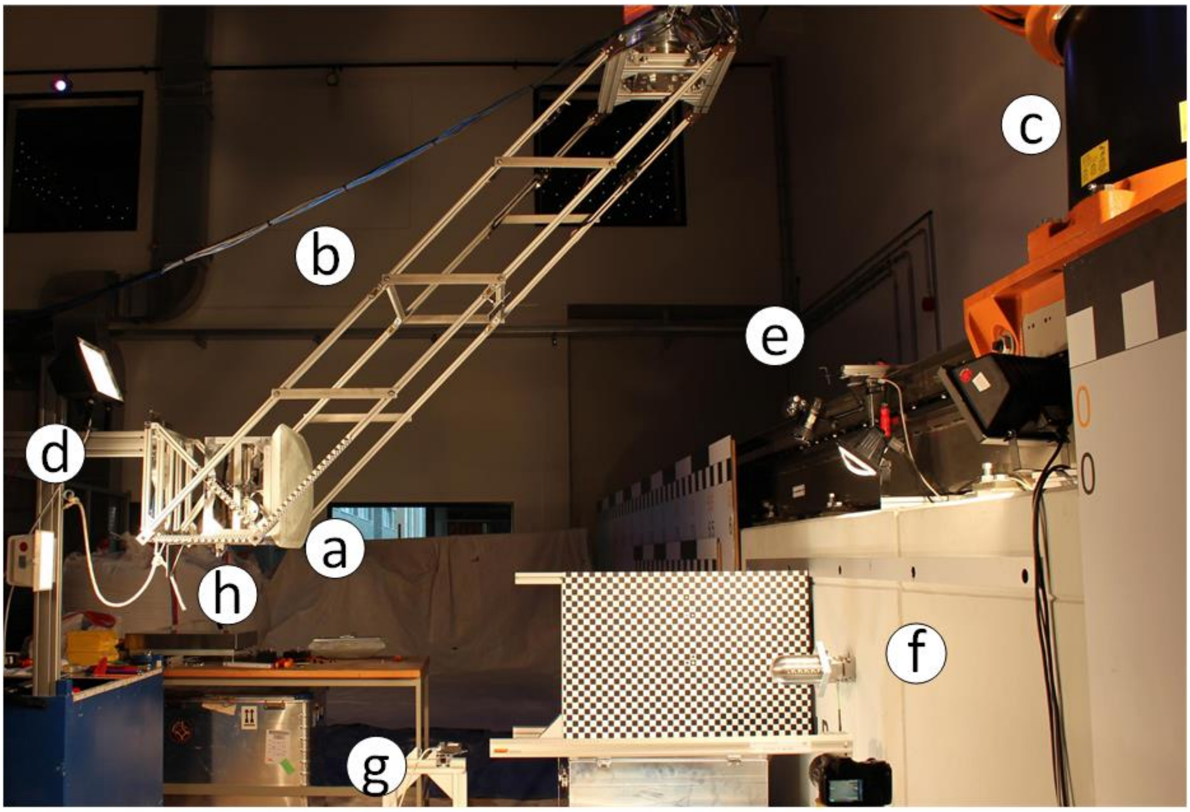

Fig. 4-1: Pendulum test rig at the Landing & Mobility Test Facility (LAMA). a) The lander dummy with its crash-pad sample is integrated in b) a rigid parallel bar pendulum which is attached to c) a KUKA KR500 robot and hold by d) an electro-magnet. e) The upper laser sensor measures pendulum bending and oscillations, while f) the deflector (flat)/penetrator target measures impact force, g) the lower laser the specimen trajectory and h) a 3-axis accelerometer the impact accelerations.

Impact tests with crash cushions were performed on the two different impact obstacles: (i) a flat surface and (ii) an obstacle with an idealized, hemispherical stone ("penetrator"). All tests here had a common impact velocity of 4 m/s. Table 4-1 summarizes the test and comparison cases. The honeycomb comparison tests carry the suffix 'HC'.

Table 4-1: Tests for comparison.

No.	Test case	Material	Type	Target	Crush force [kN]
1	Case_01-Side_4_flat	SS316L	Lattice	Flat	3.9
1HC	Case03-SS5-GFK-5052-DEF	PACL-XR1-0.6-3/4-07-P-5052	Honeycomb	Flat	3.0
2	Case_02-Side_4_pen	SS316L	Lattice	Penetrator	2.8
2HC	Case06-SS7-GFK-3003-PEN	PACL-XR1-1.2-1/0-30-P-3003	Honeycomb	Penetrator	1.7

The execution of the tests is summarized in the image sequences in Fig. 4-2, which illustrate the time sequences and dimensions of the impact dynamics. These show the initial contact in each case at the time t = 0 s. The two subsequent images show the times of maximum penetration and the time of release from the obstacle. The last image of each series shows the resulting deformation image.

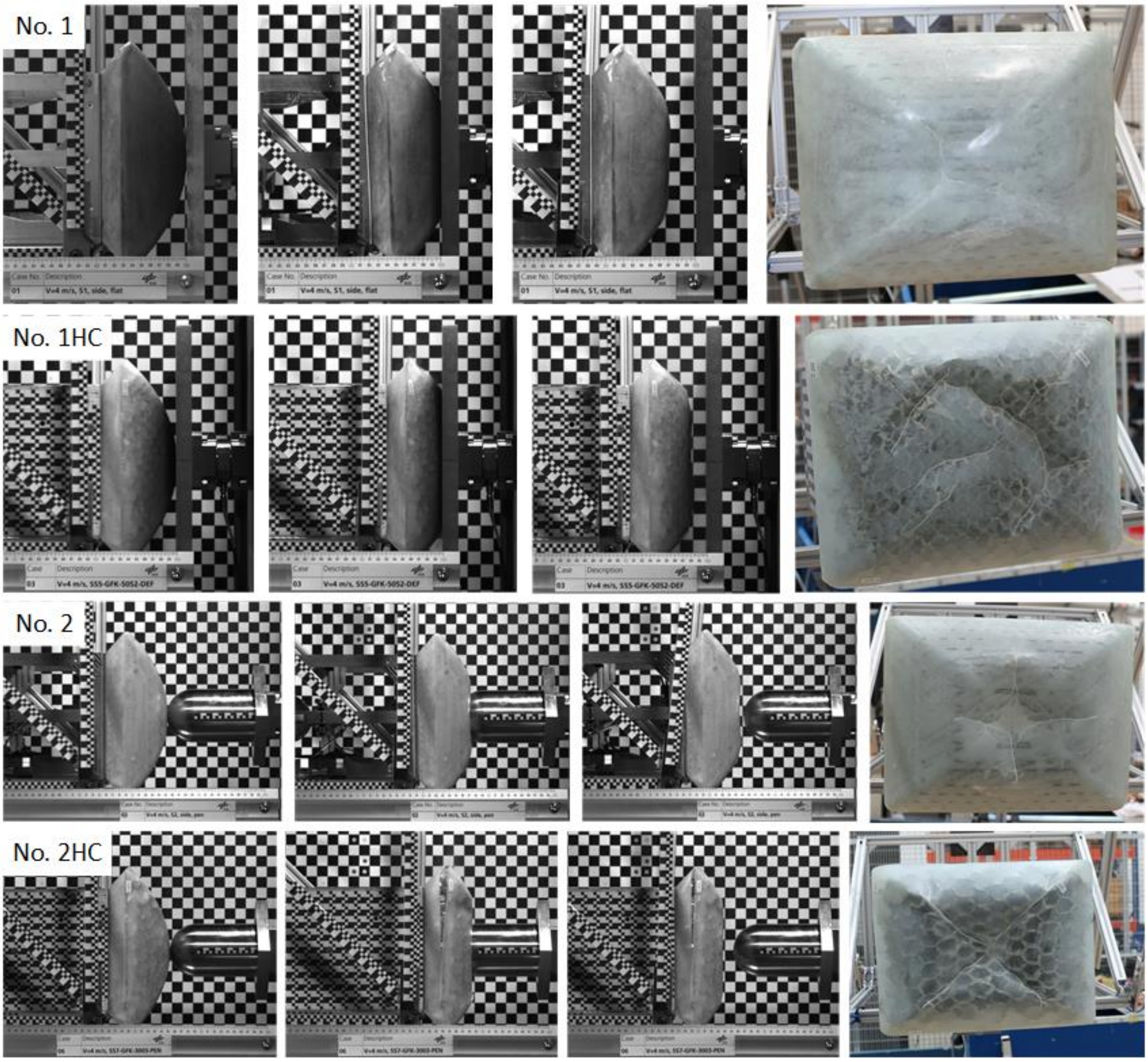

Fig. 4-2: Test sequence of Test No. 1 to 2HC.

The recorded impact force and acceleration data and the resultant penetration depth, measured as target displacement, are used for the further assessment of the sample's energy absorption characteristics and shock environment. Force -displacement curves and shock response spectra (SRS) are used subsequently therefore. The recorded raw data for force, displacement and acceleration is depicted as well as time series data in Annex B.

The force -displacement curves shown in Fig. 4-3 are characteristic off the energy absorption behavior of the cushions. The corresponding measured values are shown in Table 4-1. Compared to the flat target, the penetrator generates a locally more limited contact zone and thus, for a given material thickness (crush strength), a lower crush force than the comparable flat contact. The impact energy is correspondingly dissipated over a longer distance. The surface areas below the curves are (almost) the same (same energy dissipation). Furthermore, comparing the crush force between the different materials used for the cushion core the curves are similar, but the slope of the printed structure is steeper, which implies a higher crush strength, other than expected in Fig. 2-7. The analysis of this behavior is done in chapter 5.

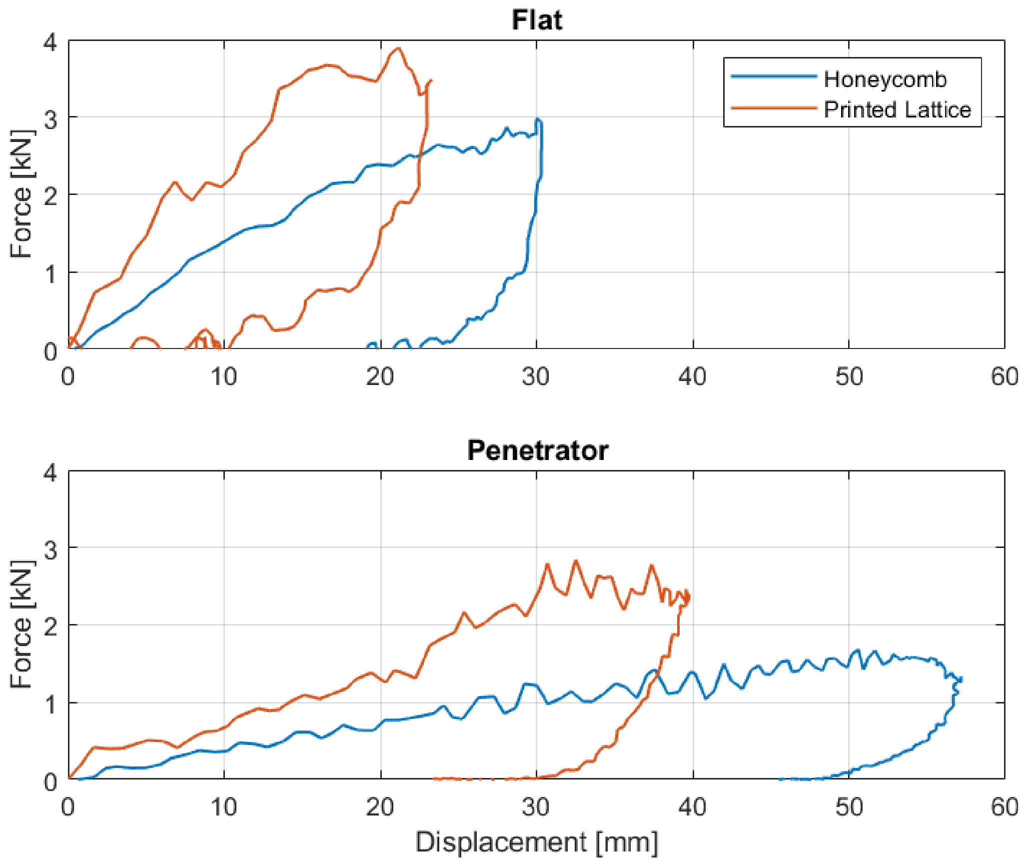

Fig. 4-3: Force-Displacement curves of presented pendulum tests.

The sudden deceleration of the impact creates a shock environment for the lander body. A shock response spectrum (Fig. 4-4) has been derived from the acceleration time series data in order to analyze its frequency content. The acceleration level of both the flat and the penetrator target is higher with the printed lattice structure than the honeycomb-made absorbers. This is as expected due to the higher crush strength of the 3D-printed core. Again, the shape of the curves is similar between the printed and the honeycomb absorbers. The acceleration level of the printed absorber during a flat contact is generally higher than for the penetrator due to its larger contact patch, and results in a nearly flat profile of ~100 g across the frequency domain. In that regard, the penetrator exhibits an increasing acceleration level for printed absorbers starting at approximately ~50 g and rises to ~100 g at 600 Hz. The honeycomb cushion, on the other hand, peaks with ~70 g at ~450 Hz but stays below 50 g across the remaining frequency domain.

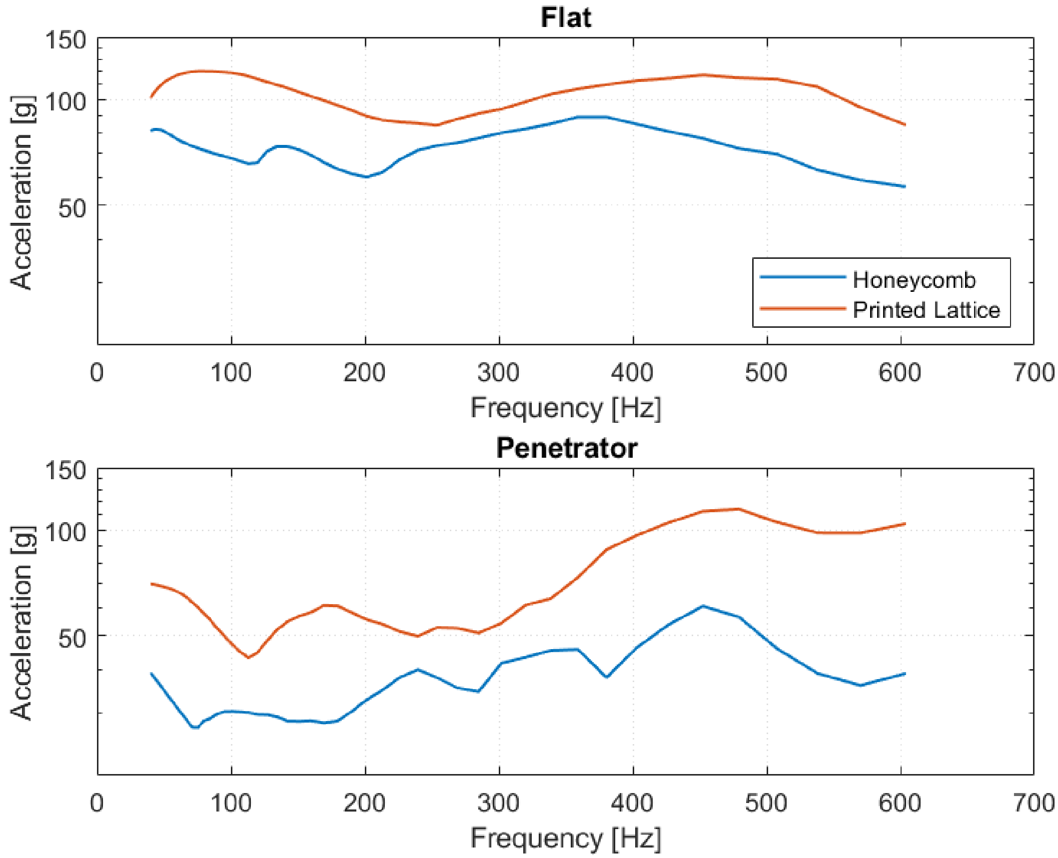

Fig. 4-4: Shock response spectrum of presented pendulum tests.

5. Discussion and results

The investigations performed have shown the feasibility of 3D-printed lattice structures for use as energy-absorbing protection. The resulting crush strength of the stainless-steel lattices matched the lowest values of commercially available crushable honeycomb grades, and even lower crush strengths are possible with available printer technology. The bulk density of the printed lattice samples produced is still inferior to comparable honeycomb material. This is largely attributable to the use of steel alloys to achieve the necessary ductile material behavior. The density was reduced already within this study by an optimized lattice unit cell. Advances in the heat treatment of printable aluminum alloys have not been pursued in this study, but are a means to further reduce the mass of printed energy absorbers. Compared to aluminum honeycomb, printed structures have the advantage of being manufactured even to dedicated arbitrary shapes and becoming conformal energy-absorbing shells. In comparison, the delicate foils of the low crush strength honeycomb become difficult to machine into complex shapes. They do not allow vacuum molding for curing of the additional face sheets. Tests have shown comparable load- and shock-absorbing characteristics between honeycomb and printed lattice structures, although the loads seen when using the latter have been higher. This is attributable to the non-isotropy of the printed lattice when loaded along its beams.

Using a face-sheet spreads the load onto a wider area and stabilizes and constraints the entire lattice on its sides, therefore producing a multiaxial load transmission (see Fig. 5-1) in comparison to the uniaxial load case in Fig. 2-5.

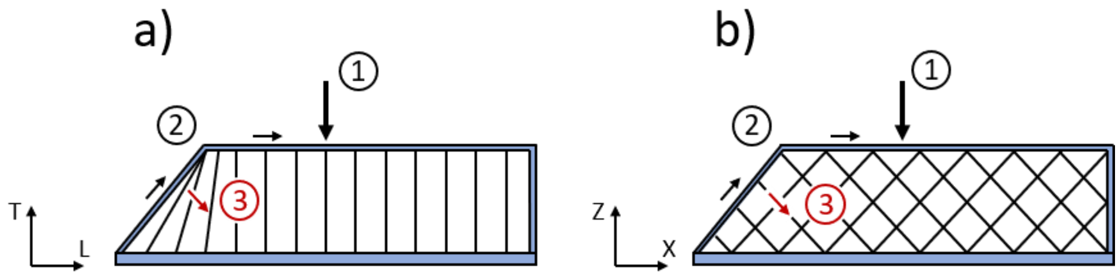

Fig. 5-1: Comparison of a crushable sandwich with surrounding face-sheet: a) Core of aluminum honeycomb, b) Core of a 3d printed lattice. (1) Main load introduction, (2) Tensioning of face-sheet, (3) Resulting lateral load component

Whereas for the honeycomb, the main load is introduced in its strong axis T (cell direction) and the resulting lateral loads via the contracting face-sheet are introduced in the much weaker L and W direction. For the printed lattice, it seems to be the exact opposite. Here the load is primarily introduced in its weaker axis and the resulting lateral loads via the contracting face-sheet are introduced in its stronger 45-degree angled axes. As a consequence, and even if the printed sample tests show a lower compressive strength as compared to the honeycomb, with the combination of the face-sheet the global stiffness of the cushion is much higher. Consequently, the deceleration of the specimen happens in a much shorter distance and time resulting in a much higher load response. The general literature [13],[14],[15] so far only deals with local failure modes of sandwich designs. A first study of the global effects of face-sheets for small cushions, like the one presented here, can be found in [16]. Continuative studies regarding crushing behavior of metal lattice structures can be found in [17],[18],[19].

Mitigation was not pursued in this study, but could be achieved by printing these beams with an initial "S" or "C"-curve to facilitate an earlier buckling onset (Fig. 5-2). This measure would be equivalent to the pre-crushing of aluminum honeycomb material, which is typically used to overcome its initial force peak.

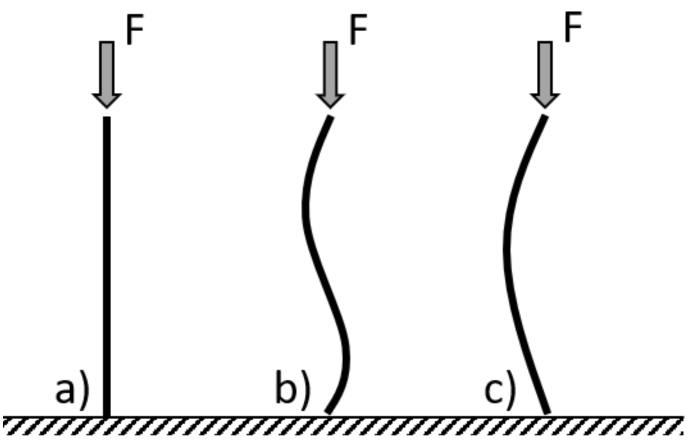

Fig. 5-2: Curved beam design for an adapted unit cell, which enables easy buckling:
a) straight beam, b) beam with an S-curve, c) beam with a C-curve.

This study has been carried out in the context of an impact load attenuation system for small planetary landing probes. Whether aluminum honeycomb or printed lattice energy-absorbing structures will be used is subject to system-level trade-off studies, which have to balance the advantages and disadvantages between mass, performance and manufacturability. An open point is the influence of welding four quarters to one whole cushion, which was necessary as the available printers were too small. This effect could not be studied within the scope of this project.

6. Conclusion

Of the three printable metallic materials available, stainless steel was the only one that was ductile enough to bend under load, while the aluminum and titanium grids broke during compression. The chosen lattice structures were simple diagonal beams of 1 mm diameter. The unit cell size was adjusted to the given use case (here the touchdown of a small lander on a moon) and was set to 23 mm.

The test runs have been compared with classic honeycomb crash cushions, which were also tested on the same test stand at DLR. The results have shown a similar behavior, with a slightly better performance of the honeycomb structures, which are also more mass-efficient.

Nevertheless, when it comes down to very small crush strengths, the available honeycomb materials come to an end. 3D printed metal grids could be produced in arbitrary sizes. Their crush strength would then be limited only by the size of the printer volume.

Funding

This work was supported by Wirtschaftsförderung Bremen GmbH [grant number: LURAFO1003A].

CRediT authorship contribution statement

Silvio Schröder: Conceptualization, Methodology, Validation, Investigation, Resources, Writing – original draft, Writing – review & editing, Visualization, Project administration, Funding acquisition. **Christian Grimm:** Investigation, Formal analysis, Data curation, Writing – review & editing, Visualization. **Lars Witte:** Conceptualization, Formal analysis, Resources, Writing – review & editing. **Adli Dimassi:** Software, Validation, Writing – review & editing, Visualization. **Philip Buchholz:** Software, Resources, Writing – review & editing, Visualization.

Declaration of Competing Interest

The authors declare that they have no known competing financial interests or personal relationships that could have appeared to influence the work reported in this paper.

7. References

[1] C. Yang C, Q.M. Li, Structural optimisation for the collapse zone of a railway vehicle, International Journal of Mechanical Sciences, 2020. https://doi.org/10.1016/j.ijmecsci.2019.105201

[2] S. Kokkula et al., Offset impact behaviour of bumper beam–longitudinal systems, International Journal of Crashworthiness,2005. http://dx.doi.org/10.1533/ijcr.2005.0106

[3] O. Ganilova, J. Low, Application of smart honeycomb structures for automotive passive safety, Proceedings of the Institution of Mechanical Engineers, Part D: Journal of Automobile Engineering. Vol. 232. 2017. https://doi.org/10.1177/0954407017708916

[4] CYMAT, Aluminum Foam Technology Applied to Automotive Design, Company handbook, 2019. https://www.cymat.com/wp-content/uploads/2019/05/Cymat_SAF_Automotive_Applications-2.pdf

[5] K. Kremer, Metal Foams for Improved Crash Energy Absorption in Passenger Equipment, Fraunhofer USA, Newark, DE, 2004. http://onlinepubs.trb.org/onlinepubs/archive/studies/idea/finalreports/highspeedrail/hsr-34final_report.pdf

[6] C. Yang, Management of Impact Energy and Shock in Rail Crash, Department of Mechanical, Aerospace & Civil Engineering, Student thesis: Phd, Manchester, 2020. https://pure.manchester.ac.uk/ws/portalfiles/portal/208485290/FULL_TEXT.PDF

[7] S. Timoshenko, et.al, Theory of Plates and Shells (2nd Edition), McGraw-Hill Book Company, USA, 1959, ISBN 0-07-064779-8 https://www.academia.edu/37205290/Theory_of_Plates_and_Shells_2nd_Edition_Timoshenko_and_S_Woinowsky_Krieger_pdf

[8] A. Rajaneesh, et.al, Indentation failure of circular composite sandwich plates, Materials & Design, 2016. https://doi.org/10.1016/j.matdes.2015.09.070

[9] S. Megahed, et.al, Effect of Heat Treatment on Ductility and Precipitation Size of Additively Manufactured AlSi10Mg. Metals 2022, 12, 1311. https://doi.org/10.3390/met12081311

[10] Jeon, S.-Y., Synergistic Energy Absorption Mechanisms of Architected Liquid Crystal Elastomers, Adv. Mater. 2022, 2200272, https://doi.org/10.1002/adma.202200272

[11] 3-matic User manual, https://s3.amazonaws.com/helpjuice-static/helpjuice_production%2Fuploads%2Fupload%2Fimage%2F5908%2Fdirect%2F1578074370812-3-matic+14.0+-+User+Manual.pdf

[12] S. Schröder, et.al, A crushable shell for small body landers, CEAS Space Journal, https://doi.org/10.1007/s12567-019-00261-z

[13] T. N. Bitzer, Honeycomb Technology: Materials, Design, Manufacturing, Applications and Testing, Springer Science & Business Media, 1997

[14] D. Zenkert, The Handbook of Sandwich Construction, Engineering Materials Advisory Services, 1997 [p.130]

[15] L. J. Gibson, et.al, Cellular Solids: Structure and Properties, 2nd ed. Press Syndicate of the University of Cambridge, Cambridge, UK, 1997, https://doi.org/10.1017/CBO9781139878326

[16] C. Grimm, Methodology for the Design and Verification of Small Body Landers with a Crushable Impact Absorber, Dissertation, University of Bremen, 2023

[17] R. Gümrük, et.al, Static mechanical behaviours of stainless steel micro-lattice structures under different loading conditions, Materials Science and Engineering: A, Volume 586, 1 December 2013, Pages 392-406, https://doi.org/10.1016/j.msea.2013.07.070

[18] C. Li, et.al, Crushing behavior of multi-layer metal lattice panel fabricated by selective laser melting, International Journal of Mechanical Sciences, Volume 145, 2018, Pages 389-399, ISSN 0020-7403, https://doi.org/10.1016/j.ijmecsci.2018.07.029

[19] Zuhal Ozdemir, et.al, Energy absorption in lattice structures in dynamics: Experiments, International Journal of Impact Engineering, Volume 89, 2016, Pages 49-61, ISSN 0734-743X, https://doi.org/10.1016/j.ijimpeng.2015.10.007

[20] Plascore, CrushLite-Sheet-Metric, Company datasheet, 2021. https://www.plascore.com/download/datasheets/energy_absorption_documentation/Plascore_CrushLite-Sheet-Metric-2021_2.pdf

[21] EuroComposites, Aluminum Honeycomb Core, Company datasheet, 2013. https://www.nzcomposites.com/site/nzcomposites/Aluminium%20Honeycomb%20Core.pdf

[22] Corex, Corex-Data-Sheet-160mm-fold-English-WEB, Company datasheet, 2021 https://de.scribd.com/document/500882357/Corex-Data-Sheet-160mm-Fold-English-WEB-pdf

[23] Alcore, TheGillCorp_DURA-CORE II 5052, Company datasheet, 2020. https://www.thegillcorp.com/alcore/DURA-CORE%20II%205052.pdf

[24] Hexcel, HexWeb CR III, Company datasheet, 2017. https://fileserver.mates.it/Prodotti/4_Anime/TDS/Hexcel/CRIII_US_DS.pdf

8. Annex A

Table 8-1: Aluminum 3003 honeycomb; data has been summarized from following sources: Plascore [20], EuroComposites [21], Corex [22]

Manufacturer	Type/Grade	Bulk density [kg/m³]	Crush strength [MPa]
Plascore	CrushLite PACL-XR1	16.0	0.07
Plascore	CrushLite PACL-XR1	22.4	0.17
EuroComposites	ECM	29	0.26
Plascore	CrushLite PACL-XR1	28.8	0.31
Corex	3000 series	41.6	0.41
EuroComposites	ECM	41	0.58
EuroComposites	ECM	55	0.89
Plascore	CrushLite PACL-XR1	57.7	0.83
EuroComposites	ECM	77	1.68
EuroComposites	ECM	82	1.67
Plascore	CrushLite PACL-XR1	83.3	1.69
EuroComposites	ECM	130	3.38

Table 8-2: Aluminum 5052 honeycomb, data has been summarized from: Plascore [20], Alcore [23], Hexcel [24]

Manufacturer	Type/Grade	Bulk density [kg/m³]	Crush strength [MPa]
Plascore	CrushLite PACL-XR1	9.61	0.0517
Alcore, Gill Corp.	PAA-Core	12.81	0.1034
Hexcel	HexWeb CR III	16.02	0.1724

Hexcel	HexWeb CR III	25.63	0.2758
Hexcel	HexWeb CR III	32.04	0.4137
Hexcel	HexWeb CR III	36.84	0.5171
Hexcel	HexWeb CR III	41.65	0.6206
Hexcel	HexWeb CR III	48.06	0.8274
Hexcel	HexWeb CR III	49.66	0.8964
Hexcel	HexWeb CR III	54.46	1.0343
Hexcel	HexWeb CR III	59.27	1.2411
Hexcel	HexWeb CR III	60.87	1.2756
Hexcel	HexWeb CR III	67.28	1.5169
Hexcel	HexWeb CR III	68.88	1.5859
Hexcel	HexWeb CR III	70.48	1.7238
Hexcel	HexWeb CR III	72.08	1.7927
Hexcel	HexWeb CR III	83.30	2.3098
Hexcel	HexWeb CR III	84.90	2.3443
Hexcel	HexWeb CR III	86.50	2.4822
Hexcel	HexWeb CR III	91.30	2.6891
Hexcel	HexWeb CR III	96.11	2.9649
Hexcel	HexWeb CR III	97.71	3.1028
Hexcel	HexWeb CR III	104.12	3.4820
Hexcel	HexWeb CR III	110.53	3.9646
Hexcel	HexWeb CR III	126.55	4.9989
Hexcel	HexWeb CR III	129.75	5.1713
Hexcel	HexWeb CR III	134.55	5.5160

Annex B

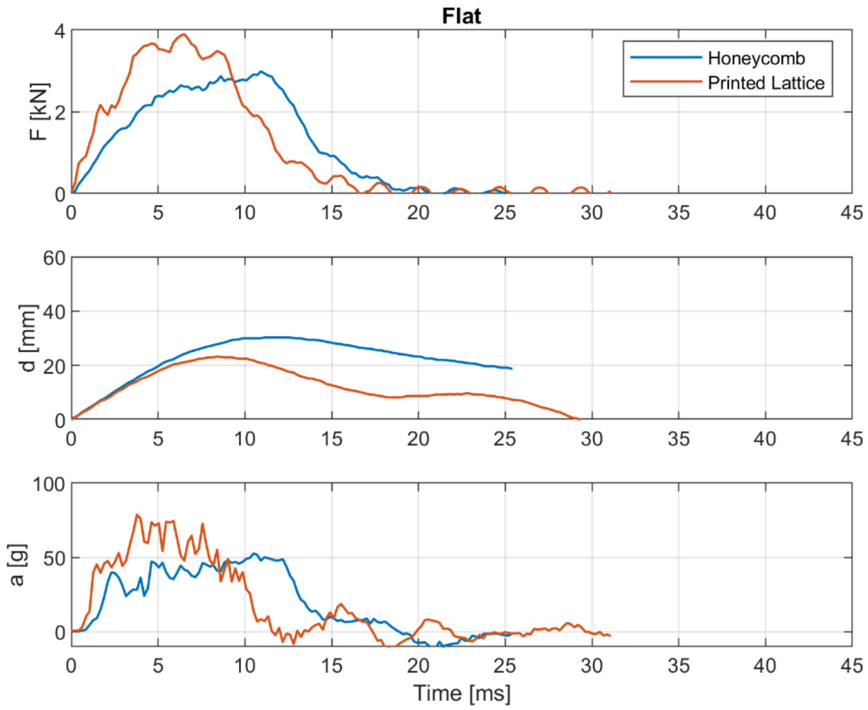

Fig. 8-1: Recorded time series data from impacts on flat target with impact force F, penetration depth (displacement) d and acceleration a.

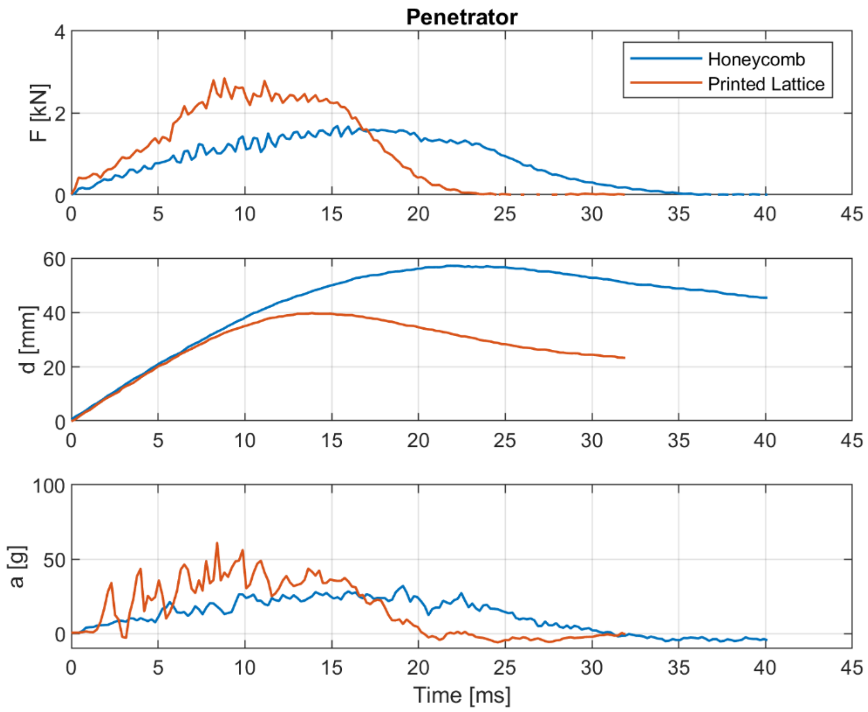

Fig. 8-2: Recorded time series data from impacts on penetrator with impact force F, penetration depth (displacement) d and acceleration a.